

Upper mantle seismic anisotropy beneath the Northern Transantarctic Mountains inferred from peridotite xenoliths near Mt. Melbourne, northern Victoria Land, Antarctica

Daeyeong Kim ^{a,*}, Munjae Park ^b, Yongcheol Park ^a, Chao Qi ^c, Hwayoung Kim ^a, Mi Jung Lee ^a, Katsuyoshi Michibayashi ^d

^a Division of Earth Sciences, Korea Polar Research Institute, Republic of Korea

^b Department of Earth and Environmental Sciences, Korea University, Republic of Korea

^c Key Laboratory of Earth and Planetary Physics, Institute of Geology and Geophysics, Chinese Academy of Sciences, Beijing, China

^d Department of Earth and Planetary Sciences, Graduate School of Environmental Studies, Nagoya University, Japan



ARTICLE INFO

Keywords:

Mantle xenolith
Mt. Melbourne
Seismic anisotropy
Olivine
Crystallographic preferred orientation
Electron backscatter diffraction

ABSTRACT

Microstructural investigations of mantle xenoliths from the Mt. Melbourne area were undertaken to reveal the origin of S-wave splitting beneath northern Victoria Land, Antarctica. The six analyzed peridotites contain various deformation features. The rotated olivine maxima of [100] and [010] into horizontal and vertical orientations, respectively, are classified into five samples with a D-type crystallographic preferred orientation (CPO) and one sample as an A-type CPO. The D-type olivine fabric can be explained by multiple slip systems of {0kl} [100] at low-temperature and high-stress conditions; therefore, both compressional and extensional regimes during subduction and rifting, respectively, could be applied in this study. With an assumption that olivine α -axes are aligned along the direction of mantle flow to form maximum S-wave splitting, the observed delay time of 0.9–1.3 s beneath northern Victoria Land can be partially explained by the anisotropy in the mantle peridotites. The remaining seismic anisotropy can be explained by the presence of melt pockets trapped along tectonic faults that developed perpendicular to the fast S-wave splitting direction. This study therefore demonstrates that the NE–SW-trending S-wave splitting beneath northern Victoria Land, Antarctica, results from the existence of both mantle peridotites as well as melt pockets trapped along the tectonic faults.

1. Introduction

Knowledge of the rheology of the Earth's interior is crucial to understanding important geological processes such as mantle convection and the thermal evolution of our planet (e.g., Karato, 2008). In the Earth's upper mantle, plastic deformation of mantle materials results in an anisotropic microstructure that usually occurs via the development of crystallographic preferred orientations (CPOs). As the major mineral in the upper mantle, olivine, is strongly anisotropic, the anisotropy in its microstructure induces an anisotropy in the propagation of seismic waves and can be documented by seismic observations. Thus, the study of seismic anisotropy is a powerful tool for understanding the evolution of the upper mantle, mantle flow patterns, mantle dynamics, and tectonics (Ben Ismaïl and Mainprice, 1998; Hess, 1964; Jung and Karato, 2001; Jung et al., 2006; Karato et al., 2008; Long, 2013; Long and Silver,

2009; Mainprice, 2007; Nicolas and Christensen, 1987; Savage, 1999; Silver, 1996; Skemer and Hansen, 2016; Tommasi and Vauchez, 2015).

Plastic deformation of olivine at different mantle conditions activates a variety of slip systems and induces different mechanisms for CPO formation, such as deformation-induced lattice rotation, grain boundary migration (Karato, 2008) and grain shape preferred orientation (Miyazaki et al., 2013), thereby resulting in different CPO patterns. Observations on olivine rocks deformed in natural systems and experimentally deformed in laboratory settings at high pressures high temperatures have revealed six types of CPOs (A–E and AG) in olivine (Holtzman et al., 2003; Jung and Karato, 2001; Jung et al., 2006; Katayama et al., 2004; Katayama and Karato, 2006; Mainprice, 2007). Deformation experiments and numerical models suggest that the formation of olivine CPO is controlled mainly by stress, temperature, and water contents (Karato et al., 2008), but is also affected by other prevailing factors such as

* Corresponding author. Division of Earth Sciences, Korea Polar Research Institute (KOPRI), 26 Songdomirae-ro, Yeonsu-gu, Incheon, 21990, Republic of Korea.
E-mail address: dkim@kopri.re.kr (D. Kim).

deformation geometry (Tommasi et al., 1999), the existence of partial melts (Holtzman et al., 2003; Qi et al., 2018), grain shape alignment during diffusion creep with the presence of secondary phases (Miyazaki and Hiraga, 2017; Miyazaki et al., 2013; Soustelle and Mantelake, 2017; Sundberg and Cooper, 2008), and deformation history (Bernard et al., 2019; Boneh et al., 2015; Boneh and Skemer, 2014; Kumamoto et al., 2019). The relationship between the CPO patterns of olivine and its conditions of formation in the mantle has also been applied to studies of natural mantle rocks and has aided the interpretations of mantle dynamics (Cao et al., 2015; Karato et al., 2008).

Northern Victoria Land, Antarctica has experienced a series of tectonic events, including subduction and rifting, and the mantle flow beneath it reveals the dominant role of the mantle (mantle plumes or small-scale mantle convection) in the formation of the Transantarctic Mountains (Armienti and Perinelli, 2010; Faccenna et al., 2008; Kyle et al., 1992; Rocchi et al., 2002, 2003, 2005). The observed seismic anisotropy beneath northern Victoria Land, Antarctica shows widespread fast S-wave polarization along a NE-SW direction (Fig. 1), which differs from the direction of absolute plate motion (APM) and is interpreted to represent a lithospheric fabric formed during the Ross orogeny

(Barklage et al., 2009; Graw and Hansen, 2017; Pondrelli et al., 2006; Salimbeni et al., 2010). Scattered shear wave splitting around the David Glacier and minor polarization in the Ross Sea coastline are explained as the products of regional tectonic events, such as the formation of the Terror Rift (Graw and Hansen, 2017; Salimbeni et al., 2010). Although seismological investigations have inferred a lithospheric fabric as the origin of the anisotropy, there is no direct evidence for this explanation from mantle rocks in this area. In this study, we document microstructures and petrofabrics in mantle xenoliths from the Mt. Melbourne area in northern Victoria Land, Antarctica. Together with the equilibrium temperature of the mantle xenoliths, we calculate their seismic properties using EBSD data and discuss the generation of S-wave polarization in the region and its geological implications.

2. Geological background

The geological evolution of Victoria Land involved several episodes of Phanerozoic tectonic events. The Ross Orogen and NW-SE- to NNW-SSE-striking tectonic discontinuities within the Transantarctic Mountains were formed by the subduction of the oceanic lithosphere beneath the paleo-Pacific margin of Gondwana during the early Paleozoic (Borg et al., 1987; Finn et al., 1999; Gibson and Wright, 1985; Rocchi et al., 1998). During the Devonian to Triassic, the Kukri Peneplain developed following the Paleozoic Ross Orogen, and this was followed by Jurassic magmatism (Schmidt and Rowley, 1986; Storey and Alabaster, 1991). Amagmatic rifting occurred during the Cretaceous with the formation of four elongate N-S-trending basins in the Ross Sea and widespread denudation of the Transantarctic Mountains (Fitzgerald, 1994; Fitzgerald and Stump, 1997; Stump and Fitzgerald, 1992). Widespread magmatic activity produced plutonic complexes, dike swarms, and volcanoes during the Cenozoic (Rocchi et al., 2002). The Meander Intrusive Group includes intrusive and subvolcanic bodies, and the McMurdo Volcanic Group comprises eruptive products that contain xenoliths of ultramafic rocks (Kyle, 1990).

The Melbourne province, which is a part of the McMurdo Volcanic Group, contains active volcanoes such as Mt Melbourne, Mt Rittman, and the Pleiades in northern Victoria Land (Fig. 1). These volcanoes are generally regarded as genetically related to extensional alkalic magmatism in the West Antarctic Rift System that developed during the Late Cretaceous (DiVenere et al., 1994; Luyendyk et al., 1996). Mount Melbourne is an elongate N-S-trending stratovolcano located ~30 km northeast of Jang Bogo Station (Fig. 1). Its latest eruption occurred in either 1862–1922 CE, as estimated from snow accumulation rates and the depth of burial of ash layers in ice cliffs (Lyon, 1986), or at ~1280 CE, based on comparisons of the major element compositions of tephra layers in ice cores from over the last 10,000 years (Lee and Lee, 2017). Recent volcanic activity, including fumarole ice towers and pinnacles, has been observed in the summit area (Nathan and Schulte, 1967). Seismological observations in northern Victoria Land show a general trend of NE-SW-oriented fast S-wave polarization with an average delay time of 0.9 ± 0.04 s originated from lithosphere evaluated to be 81–135 km thick (Fig. 1) (Barklage et al., 2009; Graw and Hansen, 2017; Pondrelli et al., 2006; Salimbeni et al., 2010). APM is toward NNW-SSE (Fig. 1) (Gripp and Gordon, 2002).

The generation and evolution of the lithospheric mantle in Victoria Land have been investigated using chemical analyses of volcanic rocks and mantle xenoliths (e.g., Martin et al., 2015). The major and trace element compositions of Cenozoic basalts are similar to those of ocean island basalt (OIB), with enrichment in most incompatible elements (Nardini et al., 2009). $^3\text{He}/^4\text{He}$ ratios of crushed olivine, which are similar to those in lithospheric mantle and mid-ocean ridge basalts (MORB), and the HIMU-like whole-rock isotopic signature of the mantle source exclude a plume-driven model. Nardini et al., 2009 proposed a model to generate an appropriate mantle source in which lithospheric domains were strongly metasomatized by small amounts of melt during the Cretaceous amagmatic extension, followed by the eruption of

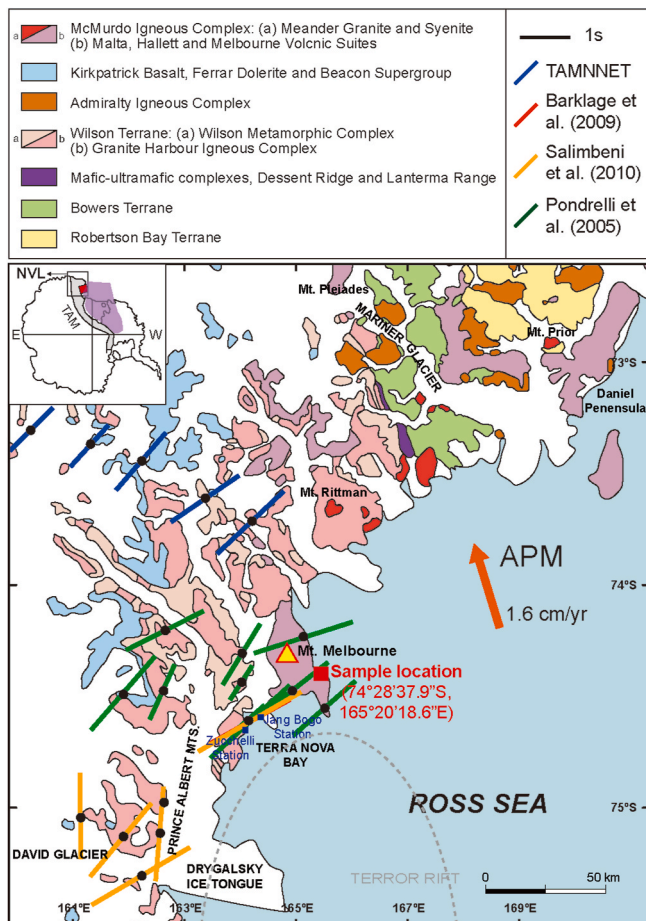


Fig. 1. Geological map of the Mt. Melbourne area, northern Victoria Land (NVL), Antarctica, showing the location of the studied mantle xenoliths. The rectangle in the upper left figure indicates northern Victoria Land in Antarctica. The grey region crossing the Antarctic continent and purple shaded area in the upper left figure denote the locations of the Transantarctic Mountains and the West Antarctic Rift System, respectively. The Mt. Melbourne area belongs to the Wilson Terrane, which is characterized by low- and medium-to high-grade metasedimentary rocks with Granite Harbour Intrusives. Absolute plate motion (APM) is from Gripp and Gordon (2002). The geological map is modified from Estrada et al. (2016). (For interpretation of the references to colour in this figure legend, the reader is referred to the Web version of this article.)

magmas along NW–SE faults. Mantle xenoliths in the area are strongly heterogeneous in terms of their whole-rock composition and mineralogy (Panter et al., 2018). Geochemical and isotopic studies (Coltorti et al., 2004; Martin et al., 2015; Melchiorre et al., 2011; Perinelli et al., 2006) indicate that the mantle xenoliths have experienced partial melting, melt–rock interactions, and mantle metasomatism.

3. Analytical techniques

The major-element compositions of olivine, orthopyroxene, clinopyroxene, and spinel were measured using a JXA-8530 field emission electron probe microanalyzer at the Korea Polar Research Institute, Incheon, Korea. Point analysis and X-ray maps were collected using an accelerating voltage of 15 kV, a beam current of 10 nA, and a beam diameter of 1 μm because of the presence of narrow clinopyroxene lamellae in orthopyroxene. Natural silicates were used as standards, and Phi-Rho-Z matrix corrections were calculated using a probe for the Electron Probe Micro Analyzer (EPMA) program.

The samples for thin sections were cut into random orientations, as the minerals in the mantle xenoliths lacked any clear structural indicators in hand specimen scales. The samples were coated with a thin layer of carbon (~ 10 nm) after mechanical and chemical polishing. Measurements were conducted by automatic indexing of electron backscatter diffraction (EBSD) patterns with an Oxford-Nordlys-HKL-EBSD on a JEOL JSM-7100F Field Emission-Scanning Electron Microscope (FE-SEM) housed at the Korea Institute for Rare Metals (KIRAM), Incheon, Korea; this microscope used an accelerating voltage of 20 kV, a step size of 50 μm , and a working distance of ~ 20 mm. The crystallographic orientation data of olivine, orthopyroxene, and clinopyroxene were measured using automatic montage mapping on whole area of the section (ca. 3.5×2.5 cm) and then the raw data were processed to compile montaged maps using the software Aztec. Noise reduction was conducted by the filling the non-indexed pixels from 8 to 5 identical neighbors using the software Channel 5 (e.g., Soustelle et al., 2013). The MATLAB toolbox MTEX was used to plot CPOs of all indexed data on lower-hemisphere equal-area projections employing ODF with half width of 20° and to calculate fabric strengths (i.e., *M*- and *J*-indices) (Bunge, 1982; Mainprice et al., 2011; Mainprice and Silver, 1993; Skemer et al., 2005). Please note that CPOs were redefined by rotating the olivine [100] (*a*-axes) and [010] maxima into horizontal (lineation) and vertical (foliation normal) directions, respectively. The shape factor (*K*) as calculated from the eigenvalues was applied to classify the shape of the crystallographic fabrics of olivine (Vollmer, 1990), and the fabric-index angle (FIA), computed from the P-wave property of a single olivine crystal, was applied for a quantitative classification of the olivine CPO types (Michibayashi et al., 2016). The software channel 5 was used to plot inverse pole figures of rotation axes contouring with a half width of 5° .

The seismic properties of olivine aggregates and mantle xenoliths (containing mostly olivine, orthopyroxene and clinopyroxene) were calculated using the program ANISctf (Mainprice, 1990), employing the densities and respective single crystal elastic constants (*Cij*) of olivine (Abramson et al., 1997), orthopyroxene (Duffy and Vaughan, 1988) and clinopyroxene (Collins and Brown, 1998) with the Voigt–Reuss–Hill averaging scheme. The P-wave seismic anisotropy (AV_P) is usually defined as the difference between the maximum and minimum velocities in two dissimilar propagating paths and is calculated using formula $200 \times (V_{P\max} - V_{P\min})/(V_{P\max} + V_{P\min})$. The S-wave seismic anisotropy (AV_S) is normally defined as the difference between two dissimilar velocities of two orthogonally polarized S-waves individually propagating through an anisotropic medium. Thus, the percentage of AV_S is $200 \times (V_{S1} - V_{S2})/(V_{S1} + V_{S2})$, in which V_{S1} and V_{S2} are the faster and slower velocities, respectively.

4. Results

4.1. Sample description and mineral chemistry

Six fresh mantle xenoliths (up to ~ 15 cm in a long axis) enveloped in vesicular basalts were collected from an outcrop located ~ 25 km from Mt Melbourne during the 2012–2013 Korean Antarctic mission ($74^\circ 28'37.9''\text{S}$, $165^\circ 20'18.6''\text{E}$; Fig. 1). The mantle peridotites are mostly massive and lack any clear foliation or lineation in hand specimens. The peridotites are classified as harzburgites and lherzolites by modal abundances as dominant assemblages of olivine (68–89 vol%) and orthopyroxene (8–26 vol%), with minor amounts of clinopyroxene (2–7 vol%) and spinel (<1 vol%) (Table 1). Microstructures of the studied peridotite xenoliths varied from an inequigranular interlobate to an amoeboid texture in three harzburgites characterized by coarse minerals and a scarcity of fine-grained recrystallized crystals. Three lherzolites show a seriate interlobate to amoeboid texture identified by a high abundance of fine-grained recrystallized crystals (mostly olivine and less commonly pyroxene) and a clear shape-preferred orientation (see the nomenclature of Moore, 1970; Passchier and Trouw, 2005) (Fig. 2).

The observed grain sizes of olivine and orthopyroxene are widely diverse from 0.1 to 5 mm, while clinopyroxene and spinel are usually smaller than 400 μm . Porphyroclastic olivine commonly shows the developments of undulose extinction, subgrains, and occasionally 120° triple junctions that are characterized by complex (e.g., curvilinear, serrated, irregular and sometimes straight) grain boundaries (Figs. 2 and 3). Fine-grained olivine crystals situated between coarse olivines and/or orthopyroxenes occur regularly in lherzolites as recrystallized grains (Fig. 2b). Porphyroclastic orthopyroxene (up to ~ 6 mm) typically displays clinopyroxene lamellae, kink bands, interlobate to smoothly curved grain boundaries and weak undulose extinction (Figs. 2 and 3). Fine-grained crystals of clinopyroxene located between/within olivines and orthopyroxenes show amoeboid grain boundaries (Fig. 3d). Clinopyroxene and spinel are usually spaced as irregular interstitial phases (Figs. 2 and 3). Melt inclusions around fractures in olivine are common in all samples.

The silicate minerals have high Mg# ($100 \times \text{atomic Mg}/(\text{Mg} + \text{Fe}^{2+})$) of 89–91 for olivine, 90–92 for orthopyroxene, and 93–95 for clinopyroxene. Spinel shows a moderate depletion in Cr# ($100 \times \text{Cr}/(\text{Cr} + \text{Al})$), ranging from 16 to 24 for lherzolite, and 32 to 34 for harzburgite. Equilibrium temperatures using a Ca-in-orthopyroxene thermometer (Brey and Köhler, 1990) were 880 – 920 $^\circ\text{C}$ for harzburgite and 860 – 880 $^\circ\text{C}$ for lherzolite (Table 1), indicating that the analyzed peridotites were extracted from a relatively shallow depth. Orthopyroxene cores and rims had similar Ca contents, and lower temperatures (~ 850 $^\circ\text{C}$) were obtained from recrystallized orthopyroxene crystals. Assuming a geothermal gradient of dynamic rift (Chapman, 1986) yields a pressure of 1.0–1.5 GPa.

4.2. Crystallographic preferred orientations of olivine, orthopyroxene, and clinopyroxene

The rotated olivine CPOs in the studied mantle xenoliths present an obvious fabric (Fig. 4a). Note that the pole figures are rotated such that maxima of olivine [100] and [010] axes are horizontal and vertical, respectively. The [100] axes form a strong point maxima, while [010] and [001] axes form girdles or diffused point maxima. The distributions of [001] axes are usually the weakest. The olivine [010] axes of the three harzburgites and one lherzolite (J04-F) show a clear girdle while those of two lherzolites (J04-A5 and -C) are ambiguous. The CPO patterns in the two lherzolites are quantitatively distinguished in a later paragraph of this section and in section 4.3.

Orthopyroxene and clinopyroxene show more dispersed CPOs than olivine because of the poor indexation of pyroxene caused probably by narrow clinopyroxene lamellae in orthopyroxene, the alteration, and the

Table 1

Summary of samples and microstructural data.

Sample	Rock type	Mode (%) ^a			T (°C) ^b	Olivine		Fabric strength (CPO)		
		Ol	Opx	Cpx		Mean grain size (μm)	Aspect ratio	N ^c	M-index	J-index
J04-B2	Harzburgite	83	16	2	900	652	2.1	887	0.17	5.70
J04-D	Harzburgite	89	8	3	880	678	2.2	425	0.19	7.97
J04-E	Harzburgite	83	16	3	920	476	2.0	1102	0.13	4.09
J04-A5	Lherzolite	71	23	6	880	531	2.1	947	0.12	3.16
J04-C	Lherzolite	76	17	7	880	568	2.1	1078	0.26	8.35
J04-F	Lherzolite	68	26	5	860	444	2.2	1485	0.17	3.46

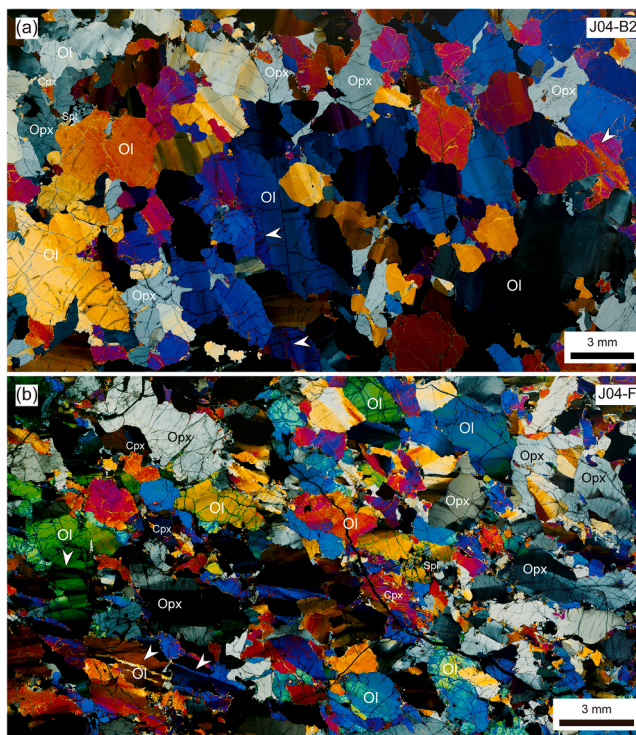
^a Modal composition modified from EBSD map without spinel (<1%).^b Temperature from Ca-in-orthopyroxene thermometer (Brey and Köhler, 1990).^c Number of indexed grains from the EBSD analysis.

Fig. 2. Cross-polarized light photomicrographs showing representative (a) harzburgite (J04-B2) distinguished by an inequigranular interlobate to amoeboid texture with coarse minerals and a scarcity of fine-grained recrystallized crystals and (b) lherzolite (J04-F) characterized by a seriate interlobate to amoeboid texture with a high abundance of fine-grained recrystallized crystals (mostly olivine and less commonly pyroxene) and a clear shape-preferred orientation. The white arrows present subgrain boundaries. Mineral abbreviations follow those of Whitney and Evans (2010).

small grain size, especially for clinopyroxene (e.g., Soustelle et al., 2013); alternately, the low abundances of these minerals in the analyzed peridotites may have also contributed to this poor indexation. Orthopyroxene in the studied peridotites tends to show the [100] axes as aligned vertically and the [001] axes as developed horizontally (Fig. 4b). Conversely, clinopyroxene displays more dispersed CPOs characterized by weak multiple clusters in most of the poles (Fig. 4c). The formation of CPOs of clinopyroxene and olivine (and orthopyroxene) in these peridotites may not have been cogenetic. The interstitial grain shapes and relatively weak CPOs of clinopyroxene suggest that they were formed at a late stage.

The grain sizes of olivine calculated from the EBSD data are estimated as 440–680 μm and are negatively correlated with the proportion of orthopyroxene + clinopyroxene (Fig. 5a and Table 1). Fabric indices (J- and M-indices) for olivine in the studied peridotites are computed as $J = 3.15\text{--}8.35$ and $M = 0.12\text{--}0.26$ and negatively correlate with the proportion of pyroxene (Fig. 5b and Table 1). The negative correlation of mean grain size and the J-index with the proportion of pyroxene has

been noted in previous studies (Morales and Tommasi, 2011; Soustelle et al., 2010, 2013). The fabric indices for orthopyroxene and clinopyroxene studied here are $J = 4.50\text{--}28.20$ and $M = 0.07\text{--}0.34$ for orthopyroxene, and $J = 4.05\text{--}6.64$ and $M = 0.03\text{--}0.09$ for clinopyroxene, with no clear relationship with lithology or mineral content. The M-index of clinopyroxene shows the lowest value (0.03–0.09) among the minerals.

The chosen reference frame is a key factor in analyzing microstructures because of the variable shapes of internal structures in different planes (e.g., variable shapes of garnet according to orientation of planes: Bell et al., 1998). Thin sections of the analyzed peridotites were prepared in random orientations because the samples did not show a clear foliation or lineation. Olivine [100] and [010] were rotated to the horizontal (lineation) and vertical (foliation normal) directions, respectively, after the EBSD measurements. Consequently, it was necessary to clarify the rotated pole figures. The analyzed mantle xenoliths showed a clear development of olivine [100]-axis fabric and only weakly developed distribution of [001] axes, suggesting that the distribution pattern of the [010] axes had to be defined. Calculated shape

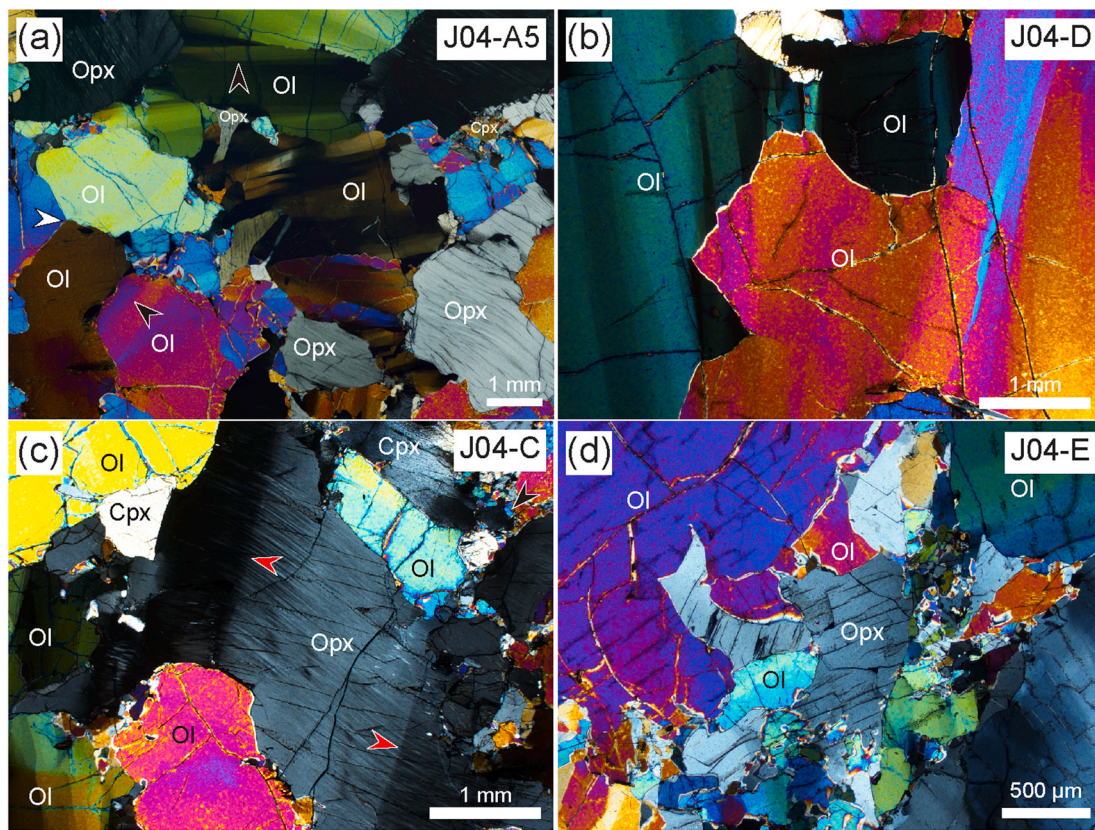


Fig. 3. Cross-polarized light photomicrographs showing representative microstructures of the analyzed spinel harzburgites and lherzolites. (a) Various shapes of olivine grains including abundant undulose extinction in sample J04-A5. The black and white arrows present subgrain boundaries and 120° grain boundaries, respectively. (b) Irregular grain boundary of olivine in sample J04-D. (c) Kink bands (red arrow) of porphyroclastic orthopyroxene in sample J04-C. (d) Microstructures of secondary olivine and orthopyroxene situated between porphyroclastic olivine and orthopyroxene in sample J04-E. Mineral abbreviations follow those of Whitney and Evans (2010). (For interpretation of the references to colour in this figure legend, the reader is referred to the Web version of this article.)

factors (K) of olivine identifying clustered (>1) or girdled crystallographic fabric are listed in Table 2 and plotted in Fig. 6. K displays most of the analyzed samples characterized by clustered [100] and girdled [010] tendencies, except for sample J04-A5, which has both girdled [100] and clustered [010] characteristics (Fig. 6a and b). The K values of [001] show variable patterns that were likely caused by the extremely weak intensity of the [001] pole (Figs. 4a and 6c). Together with the clear recognition of girdle-shaped [010] axes in harzburgites (Fig. 4a), these data indicate sample J04-A5 as recording a point maximum of [010] axes and the others as possessing a girdle of [010] axes.

Low angle boundaries ($2\text{--}10^\circ$) are analyzed by plotting inverse pole figures of rotation axes (misorientation axes) contouring with a half width of 5° (Fig. 7). The rotation axes of olivine in all the analyzed samples are distributed from [001] to [010], with the strongest intensity located in [010]. Some samples (J04-D, J04-C and J04-F) show an extremely weak intensity in [001].

4.3. Seismic properties and types of olivine

The averaged seismic properties of olivine aggregates and a rock mass composed only of olivine, orthopyroxene, and clinopyroxene are calculated by the summation of all analyzed EBSD data with averaged modal abundances for a rock mass and are plotted in Fig. 8. The figure shows that V_p maxima and maximum S-wave polarization of both olivine aggregates and a rock mass are predicted to develop along a horizontal direction, which is consistent with the orientation of the olivine α -axes' alignments (Figs. 4 and 8). The CPO pattern of the [010] axes (i.e., point maxima or a girdle) in olivine does not significantly influence the seismic properties. The calculated AV_p and AV_S of olivine

in each sample are 8.8%–9.1% and 6.7%–9.0%, respectively, with a V_p/V_S ratio of up to 1.87 (Fig. 8a and Table 3). The calculated AV_p and AV_S of a rock mass in each sample are 6.0%–10.7% and 5.1%–8.1%, respectively (Table 3), with a V_p/V_S ratio of up to 1.82 (averaged values are in Fig. 8b). Detailed seismic properties of orthopyroxene and clinopyroxene were not reported in this study because of indexation bias.

Studied olivine may be classified based on FIA, which are related to the P-wave property of single olivine crystals (Michibayashi et al., 2016). Calculations using EBSD data show FIAs of $51^\circ\text{--}76^\circ$, indicating that one sample (J04-A5) is classified as A-type olivine (orthorhombic) and the others as D-type olivine (axial-[100]) (Fig. 9 and Table 3). These results are consistent with the [010] girdle/cluster revealed by the shape factor (K), thus confirming that the classification of olivine types by shape factor and FIA methods is appropriate.

5. Discussion

5.1. Deformation conditions

Spinel peridotites around Mt. Melbourne (Barker Rocks and Greene Point) were formed by magma mixing during the Ross Orogeny and its reactivation during the opening of the West Antarctic Rift System (~ 120 Ma) (Melchiorre et al., 2011). Perinelli et al. (2006) suggested equilibrium temperatures ranging from 950 to 1050 °C and pressures of 1.0–1.5 GPa through use of a two-pyroxene geothermometer (Brey and Köhler, 1990; Wells, 1977) and an olivine-clinopyroxene Ca-exchange reaction (Brey and Köhler, 1990). Our thermometric employing Ca-in-orthopyroxene geothermometer (Brey and Köhler, 1990) estimates are relatively low (860–920 °C and 1.0–1.5 GPa) for potentially

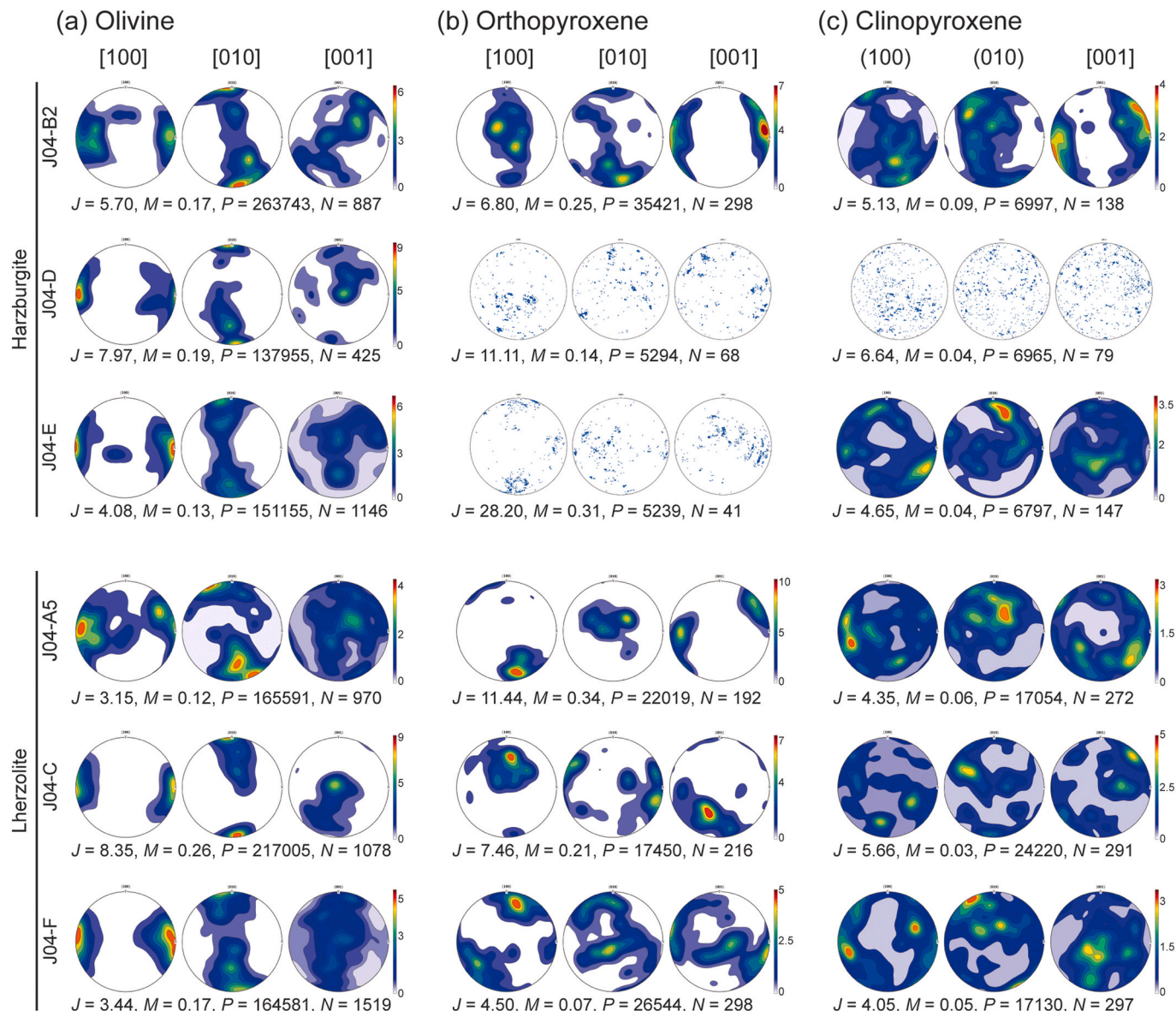


Fig. 4. Rotated crystal preferred orientations (CPOs) of olivine, orthopyroxene, and clinopyroxene in the analyzed mantle xenoliths. For preventing overestimation of strength, indexed 2000 points are plotted when N has less than 100 grains. The poles are plotted on equal-area lower-hemisphere projections using the MATLAB toolbox MTEX. The numbers in the scale indicate the pole density (multiples of uniform distribution, m.u.d.). J : J -index; M : M -index; P : analyzed pixels; N : number of analyzed grains.

forming various deformation features such as undulose extinction, subgrains of protogranular olivine and clinopyroxene lamellae, and kink bands of protogranular orthopyroxene (Falus et al., 2008; Michibayashi et al., 2007; Satsukawa and Michibayashi, 2014); thus, this topic warrants additional consideration.

Although Melchiorre et al. (2011) reported the possible presence of garnet based on highly radiogenic Hf in clinopyroxene, the studied spinel peridotites show the absence of the high-pressure aluminous phase garnet; this suggests 2.5 GPa as the maximum pressure based on the stability field of spinel, assuming temperatures lower than 1300 °C (see Fig. 13 of Perinelli et al., 2006 and references in it). The absence of low-pressure phase plagioclase yields 0.5–1.0 GPa as the minimum pressure (Green and Ringwood, 1967). The estimated temperatures and pressures of the analyzed samples calculated from a Ca-in-orthopyroxene thermometer (860–920 °C and 1.0–1.5 GPa) may indicate a ‘stagnant’ condition that is probably related with an exhumation event at low temperature and a high stress mantle shear zone (e.g., Tommasi et al., 1995). Around Mt. Melbourne, the different mineral

assemblages among spinel peridotites in this study and previous studies could be attributed to juxtaposed mantle domains along the NNW–SSE discontinuity.

5.2. Microstructures, slip systems, CPOs and deformation mechanisms

The studied mantle peridotites exhibit variable degrees of deformation by lithology. Spinel lherzolites are characterized by a large grain size, the development of shape-preferred orientation, and relatively abundant fine-grained recrystallized crystals, which is in contrast with spinel harzburgites distinguished by a larger grain size (Fig. 2). With an assumption that the proportion of pyroxene (orthopyroxene + clinopyroxene) results from the syn-kinematic percolation of Si-rich melts (e.g., Soustelle et al., 2013), the pyroxene-enrichment produces a grain size reduction, a decrease of the J -index, the development of a shape-preferred orientation, and a flexibility of grain boundary movements (Figs. 2 and 5, and Table 1). The estimated temperature in lherzolite, having enrichment in pyroxene, is slightly lower than

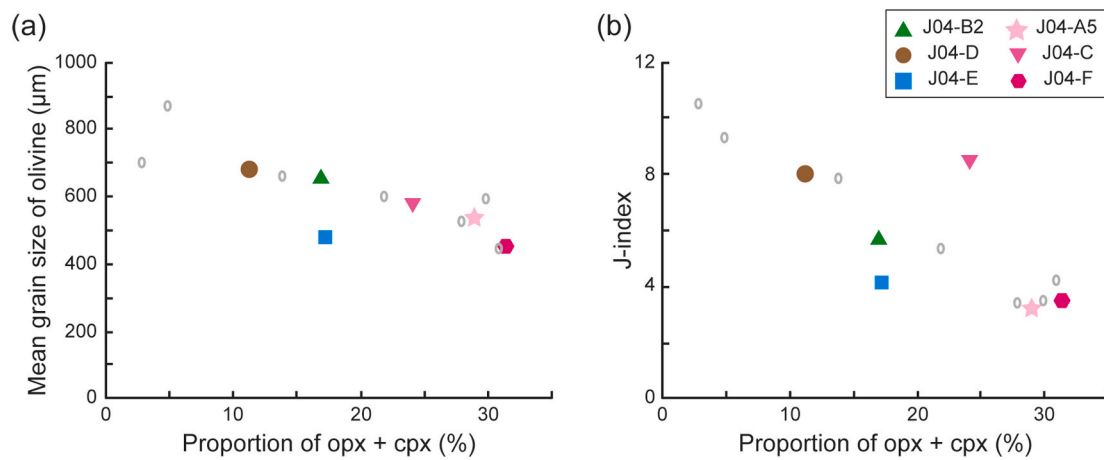


Fig. 5. Systematic decrease of (a) mean grain size and (b) *J*-index as a function of pyroxene (orthopyroxene + clinopyroxene) proportion. For comparison purposes, data from Soustelle et al. (2013) are presented as grey open circles.

Table 2

Eigenvalues and shape factor of olivine CPOs.

Sample	λ_1	λ_2	λ_3	Point	Girdle	Random	$\ln(\lambda_1/\lambda_2)$	$\ln(\lambda_2/\lambda_3)$	Shape factor, K
[100]									
J04-B2	0.648	0.210	0.142	0.506	0.137	0.425	1.126	0.394	2.860
J04-D	0.685	0.187	0.128	0.558	0.119	0.383	1.299	0.381	3.405
J04-E	0.630	0.227	0.143	0.488	0.169	0.428	1.021	0.465	2.197
J04-A5	0.585	0.286	0.129	0.456	0.313	0.388	0.716	0.794	0.901
J04-C	0.731	0.170	0.098	0.633	0.144	0.295	1.457	0.551	2.643
J04-F	0.692	0.201	0.108	0.584	0.186	0.323	1.238	0.621	1.993
[010]									
J04-B2	0.603	0.339	0.058	0.544	0.562	0.175	0.574	1.763	0.326
J04-D	0.621	0.315	0.064	0.557	0.503	0.192	0.677	1.596	0.424
J04-E	0.569	0.353	0.078	0.491	0.549	0.234	0.479	1.506	0.318
J04-A5	0.578	0.270	0.151	0.427	0.238	0.454	0.760	0.580	1.309
J04-C	0.664	0.286	0.050	0.614	0.471	0.150	0.844	1.742	0.484
J04-F	0.547	0.354	0.099	0.448	0.511	0.296	0.435	1.278	0.340
[001]									
J04-B2	0.459	0.378	0.163	0.296	0.429	0.490	0.195	0.838	0.232
J04-D	0.532	0.253	0.215	0.317	0.076	0.645	0.744	0.163	4.570
J04-E	0.445	0.318	0.237	0.208	0.164	0.710	0.335	0.297	1.127
J04-A5	0.448	0.299	0.252	0.196	0.094	0.757	0.404	0.170	2.377
J04-C	0.598	0.239	0.164	0.434	0.149	0.492	0.918	0.375	2.448
J04-F	0.446	0.352	0.202	0.244	0.301	0.605	0.236	0.557	0.424

harzburgite, thereby supporting the microstructural evolution via the pyroxene-enrichment (Table 1). Even if cryptic metasomatism has been widely reported in northern Victoria Land (Coltorti et al., 2004; Pelosso et al., 2016; Perinelli et al., 2006, 2008, 2011), the relationship between low Cr# in spinel and high Fo# in olivine indicates that the peridotites experienced low-degree partial melting, thereby implying an insignificant role for metasomatism in the studied xenoliths. The discrepancy between pyroxene-enrichment and low-degree of partial melting may suggest heterogeneity in the whole-rock composition and mineralogy (Panter et al., 2018).

In the studied peridotites, the olivine [001] is the weakest, clearly implying that [001] is unlikely the slip direction (Fig. 4a). The {0kl} [100] as the dominant slip systems of the studied olivine is also supported by a high intensity distributed from [001] to [010] of low-angle grain boundaries (Fig. 7). However, the highest intensity of rotation axes is located in [010]; therefore, (001) and [100] could be considered as slip plane and direction, respectively, in this study (Fig. 7). To consider other olivine CPOs, the highest intensity of rotation axes in [010] could indicate a (001)[100] slip system; therefore, the analyzed samples should be defined as the E-type olivine fabric rather than the A-type fabric (Fig. 7). Cao et al. (2015) explained a similar problem by the faster and more extensive consumption of dislocations of (010)[100] slip

systems compared with (001)[100] slip systems during recovery processes. Based on their approach, the slip systems of olivine must be {0kl} [100] during the deformation, as supported by the obvious girdle patterns in [010] (Figs. 4a and 6c). The {0kl} [100] slip systems of olivine are characteristic of deformation at high temperature, relatively low pressure, and variable stress (Bai et al., 1991; Cao et al., 2015; Carter and Ave'Lallmant, 1970; Couvy et al., 2004; Durham and Goetze, 1977; Jung and Karato, 2001; Jung et al., 2006; Mackwell et al., 1985; Michibayashi et al., 2016; Raterron et al., 2007). Orthopyroxene has a tendency to display a similar strength along the [100] and [001] axes, with [010] as the weakest axis, which probably implies a (100) slip plane with a [001] slip direction (Fig. 4b). The slip system of orthopyroxene (100)[001] in the analyzed spinel peridotites can be preferentially developed with low water and Al contents (Manthilake et al., 2013; Nazé et al., 1986). Orthopyroxene may show activation of the (010)[001] and (100)[010] slip systems in the moderately to weakly deformed peridotites, possibly reflecting high water and Al contents, respectively (Manthilake et al., 2013).

The olivine CPOs in the analyzed spinel peridotites are identified as D-/A-type fabric based on the shape factor (K) calculated quantitatively by eigenvalues and the FIA estimated by the P-wave property of single crystals (Figs. 6 and 9). The formation of D-type olivine has been

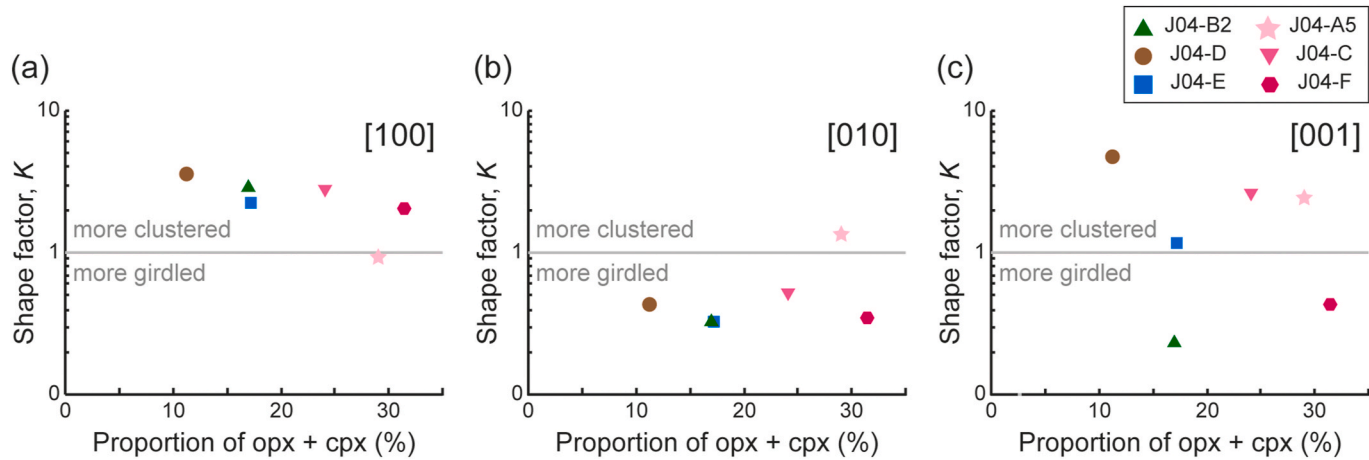


Fig. 6. Shape factor (K) of each pole of olivine calculated from eigenvalues that are computed based on Vollmer (1990).

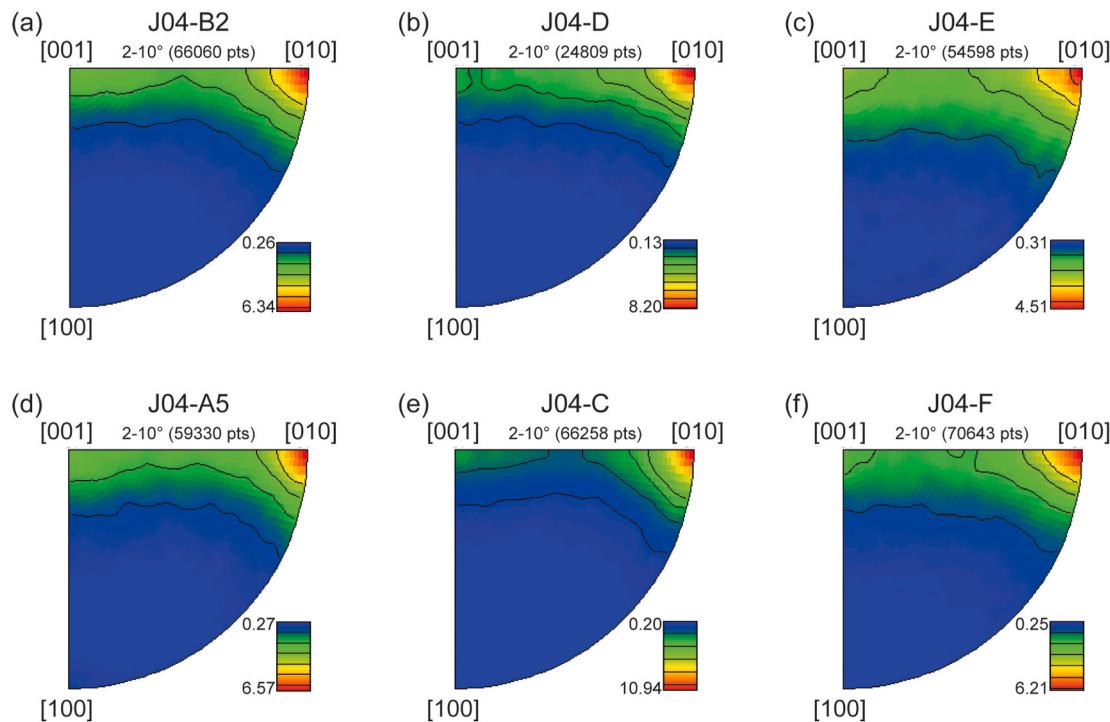


Fig. 7. Rotation axes of low-angle boundaries (2°–10°) of olivine in the analyzed mantle peridotites. All samples show the highest values in [010] with a broad intensity from [001] to [010]. Contour intervals indicated by multiples of uniform distribution (m.u.d.) are shown in legends.

explained by (1) the multiple slip systems of $\{0kl\}[100]$ at low-temperature and high-stress conditions relative to A-type olivine fabric (e.g., Cao et al., 2015), (2) the $(010)[100]$ slip system under transtensional deformation regimes (Tommasi et al., 1999), and (3) the $(010)[100]$ and $(001)[100]$ slip systems at high temperature and low stress conditions (Hansen et al., 2012, 2014a; Tommasi et al., 2000; Warren et al., 2008). Our studied samples have lower pressure-temperature limits of 1.0–1.5 GPa and 860–920 °C, a high intensity of girdled olivine [010] in the pole figure, and a high intensity from [001] to [010] in the inverse pole figure of rotation axes (Figs. 4a and 7, and Table 1); hence, the first condition (low temperature and high stress) would be preferred here. The formation of the analyzed mantle peridotite at the third condition (high-temperature and low-stress) cannot be fully excluded because of the possible genesis of McMurdo melts (Baker Rocks and Greene Point around Mt. Melbourne) at $4 \leq P \leq 5$ GPa (greater than 120 km) and 1350–1400 °C (Perinelli et al., 2006). The A-type olivine fabric

forms at high temperatures, low water contents, and low stress, as inferred from previous experiments (Hansen et al., 2012; Jung and Karato, 2001; Zhang and Karato, 1995) and natural observations (Falus et al., 2011; Michibayashi and Mainprice, 2004; Park et al., 2014).

Olivine crystals in the studied peridotites show the development of irregular grain boundaries, subgrains, and a shape-preferred orientation (Figs. 2b and 3b), thus indicating high-temperature deformation by dislocation creep. Interlobate through smoothly curved to amoeboid grain shapes are characteristic of dynamic recrystallization by grain boundary migration and grain boundary area reduction (Fig. 2). The 120° triple junctions that are occasionally observed are indicative of the post-kinematic recovery process (Fig. 3a). Coarse-grained orthopyroxene commonly displays a cooling-induced exsolution lamellae (Fig. 3c), suggesting that primary orthopyroxene is indicative of a high temperature origin. The compositional and textural characteristics of olivine and orthopyroxene suggest that both porphyroclastic minerals are primitive

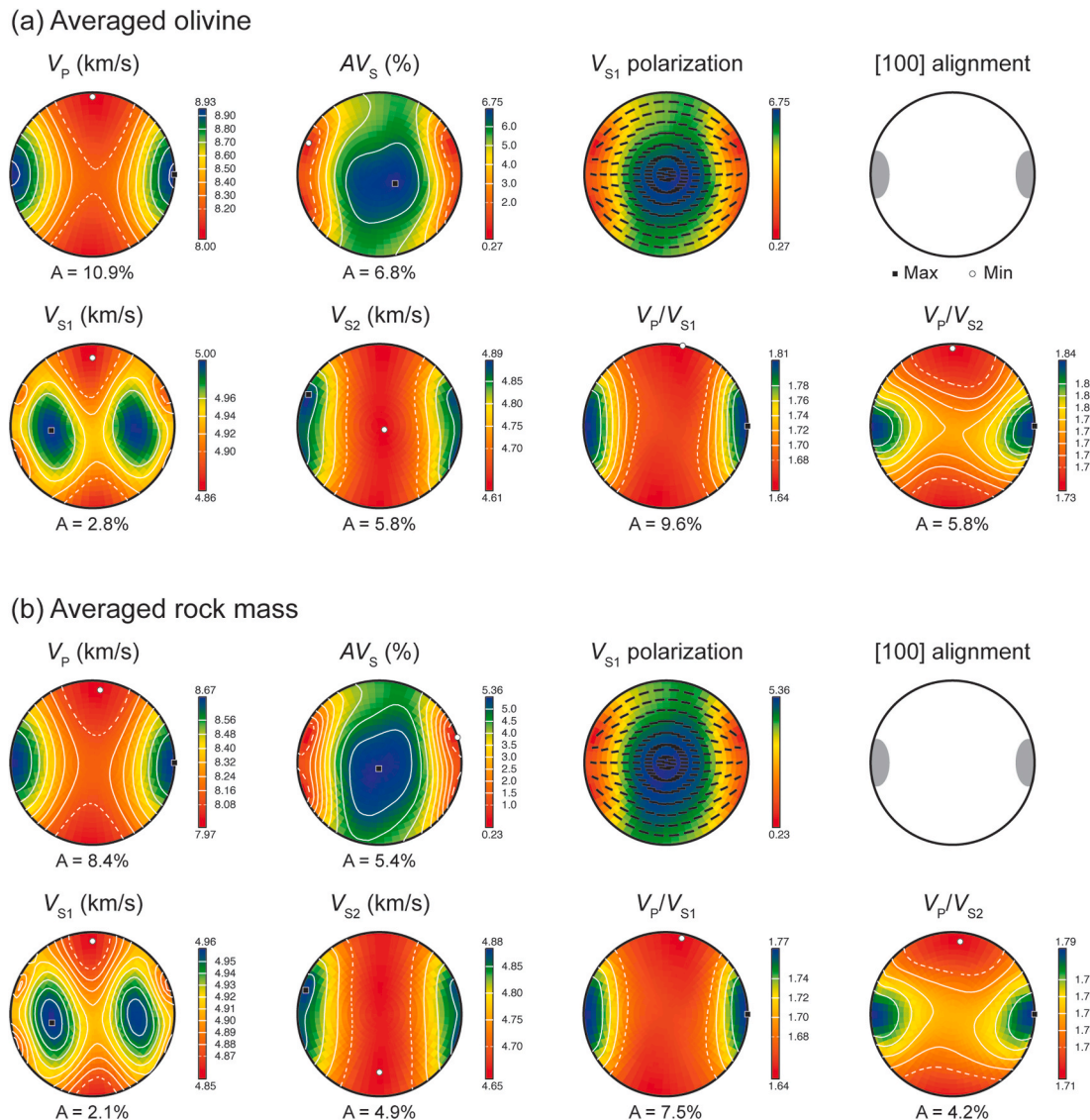


Fig. 8. Seismic properties of (a) olivine aggregates and (b) analyzed peridotites, assuming that the rock mass is composed only of olivine, orthopyroxene, and clinopyroxene. The calculation was conducted based on the summation of all data, and the mineral abundance for the rock mass was determined by averaged abundance of each rock. The properties were determined using the densities and respective single crystal elastic constants (C_{ij}) of olivine (Abramson et al., 1997), orthopyroxene (Duffy and Vaughan, 1988), and clinopyroxene (Collins and Brown, 1998) through employing a Voigt–Reuss–Hill averaging scheme. A: anisotropy.

Table 3
Summary of seismic properties of olivine aggregates.

Sample	VP_X	VP_Y	VP_Z	Seismic anisotropy (%) ⁵		FIA ⁴
				AV_P	AV_{Smax}	
J04-B2	8.92	8.20	7.98	8.9	7.62	73 (D)
J04-D	8.99	8.20	7.93	9.0	8.97	71 (D)
J04-E	8.93	8.23	7.98	8.9	6.92	69 (D)
J04-A5	8.89	8.32	7.97	8.8	6.67	51 (A)
J04-C	9.09	8.20	7.89	9.1	8.64	70 (D)
J04-F	9.00	8.17	7.97	9.1	7.74	76 (D)

in origin.

5.3. Seismic anisotropy and implications for tectonic events

Exploration of the deep Earth using S-wave anisotropy data can be powerful when combined with orientation data from minerals such as olivine in the upper mantle (e.g., Karato et al., 2008). The averaged seismic properties of both olivine and rock mass in this study show V_{Pmax}

and V_{S1} polarizations that are parallel to a horizontal direction, which is related to the alignment of olivine [100] axes (Figs. 4a and 8). Notably, maximum shear-wave splitting occurs along the alignment of olivine [100] axes (horizontal direction). The seismic properties of olivine display identical patterns but stronger characteristics than those of rock mass, indicating the dominant role of olivine in generating seismic anisotropy (Fig. 8). The V_P/V_S ratio of 1.77–1.79 in the averaged rock mass (up to 1.82 in sample J04-D) (Fig. 8b) fully satisfies the observed V_P/V_S ratio of 1.79 in a previous study (mentioned in Park et al., 2015).

To more thoroughly understand S-wave splitting in the lithospheric mantle, the thickness of anisotropic materials can be calculated using the equation $dt = AV_S/\langle V_S \rangle D$, where dt is the delay time, AV_S is the anisotropy in a specific propagation direction, $\langle V_S \rangle$ is the average of fast and slow velocities, and D is the thickness of the anisotropic layer. Fig. 10 displays the thickness of anisotropic layers composed of pure olivine and analyzed peridotites composed of olivine, orthopyroxene, and clinopyroxene. For comparison, the thicknesses of anisotropic layers composed of pure lawsonite (Kim et al., 2016), pure serpentine (Katayama et al., 2009), and polymineralic (whole-rock) peridotites (Cao et al., 2015; Soustelle et al., 2013) are also shown. In this study, an

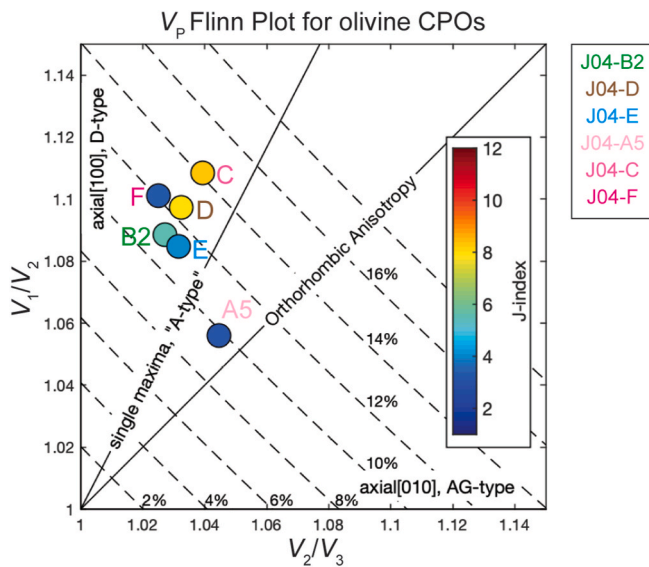


Fig. 9. A V_p Flinn diagram defining olivine types by fabric-index angles (FIAs) (Michibayashi et al., 2016). V_1 , V_2 , and V_3 denote the P-wave velocities along the X-, Y- and Z-axis of finite strain, respectively.

anisotropic layer comprising pure olivine (i.e., dunite) requires a thickness of 49–94 km, which is thicker than serpentine (10–15 km) and lawsonite (25–36 km), and weaker than olivine (95–137 km) in Katayama and Karato, 2006. On the other hand, whole-rock (i.e.,

harzburgite to lherzolite) requires a thickness of 69–123 km, that has wide range including peridotites in other studies (Cao et al., 2015; Soustelle et al., 2013). Assuming a lithospheric mantle beneath the study area with a lithospheric thickness of 100 km, the seismic anisotropy caused only by whole-rocks could partially explain the observed delay times of 0.9–1.3 s (Ponderelli and Azzara, 1998).

The studied peridotites contain clear evidence for diverse degrees of deformation. High-temperature deformation features can be described as irregular grain boundaries of porphyroclastic olivine, clinopyroxene exsolution lamellae in porphyroclastic orthopyroxene, and shape-preferred orientations of both porphyroclastic olivine and orthopyroxene (Figs. 2 and 3). Considering the limited volume of low temperature deformation features such as fine-grained recrystallized crystals and a 120° triple junction with a low degree of partial melting, a deformation during exhumation is insignificant. The D-type olivine fabric in this study is preferentially explained by the multiple slip systems of {0kl} [100] at low temperature and high stress conditions (Bystricky et al., 2000; Jung et al., 2006; Zhang et al., 2000), and it may be related with a large-scaled deformation event such as subduction or rifting (Figs. 4 and 7). The A-type olivine fabric occurred only in one of the lherzolites (sample J04-A5); this may be explained by the heterogeneous characteristics of syn-kinematic percolation of Si-rich melts during the tectonic event as related to the formation of the D-type olivine fabric, or the presence of heterogeneous post-deformation annealing associated with small-scale magmatism.

Melchiorre et al. (2011) reported highly radiogenic Os from mantle peridotites in the northern part of Mt. Melbourne (Barker Rocks and Greene Point), thereby suggesting the mixing of mafic magmas

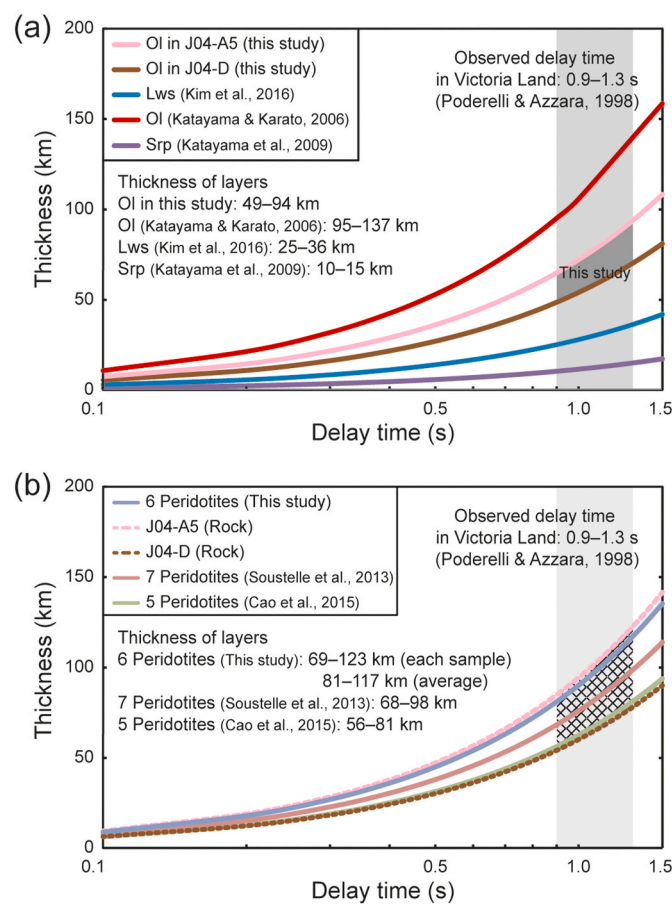
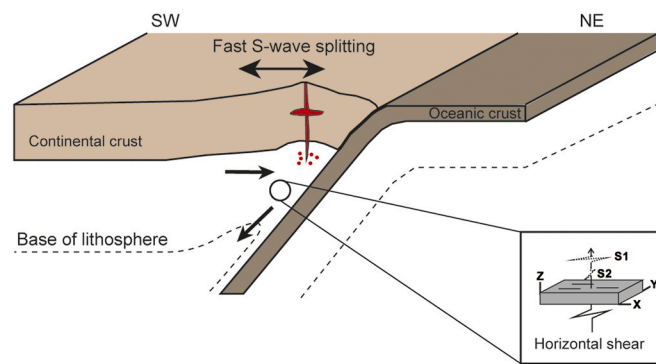


Fig. 10. Thickness of an anisotropic layer composed of (a) olivine and (b) whole-rocks versus delay time. The thicknesses of anisotropic layers composed of lawsonite ($AV_S = 14.7\%$, $\langle V_S \rangle = 4.10$ km/s; Kim et al., 2016), serpentine ($AV_S = 35.9\%$, $\langle V_S \rangle = 4.13$ km/s; Katayama et al., 2009) and olivine ($AV_S = 4.5\%$, $\langle V_S \rangle = 4.75$ km/s; Katayama and Karato, 2006) in (a), and composite rocks of peridotites ($AV_S = 6.4\%$, $\langle V_S \rangle = 4.84$ km/s; Soustelle et al., 2013, and $AV_S = 6.1\%$, $\langle V_S \rangle = 4.85$ km/s; Cao et al., 2015) in (b) are shown for comparison. For better visibility, the thickest (J04-A5) and thinnest (J04-D) values are plotted.

(a) Formation of olivine CPO by a simple corner flow



(b) Formation of olivine CPO by an extension during rifting

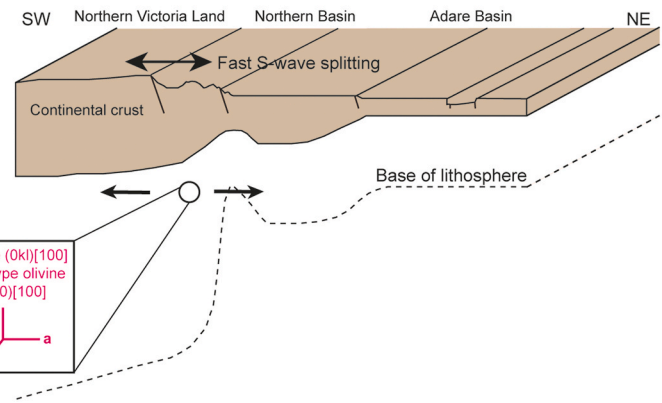


Fig. 11. Schematic models of olivine CPO formation in tectonic settings of (a) a simple corner flow in the subduction zone, and (b) extension during rifting. The models are modified from Panter et al. (2018).

characterized by 20–35% of eclogitic material during the Ross Orogeny (550–600 Ma) and the reactivation during the opening of the West Antarctic Rift System (~120 Ma). Although it is difficult to constrain the age of the analyzed samples in this study, both compressional and extensional (transtensional) regimes occurring during subduction and rifting, respectively, cannot be excluded based on low temperature and high stress conditions in the subduction zone and the presumable strong influence of metasomatism during the opening of the West Antarctic System. Based on an assumption that maximum shear-wave splitting occurs by identical alignments of olivine [100] axes and the mantle flow, two tectonic models are suggested in this study (Fig. 11). Considering the NE–SW-trending S-wave splitting with a fast polarization direction that is nearly perpendicular to the Transantarctic Mountains (Barklage et al., 2009; Graw and Hansen, 2017; Pondrelli et al., 2006; Salimbeni et al., 2010), a simple corner flow model in the subduction zone can explain the formation of the trench-perpendicular seismic anisotropy (Fig. 11a). During the formation of the West Antarctic Rift System, the extension of the lithospheric mantle could have resulted in fast shear wave splitting in the direction of mantle flow (Fig. 11b). Both models can explain the regional S-wave splitting beneath northern Victoria Land, that shows an average delay time of 0.9 ± 0.04 s generated from lithosphere estimated to be 81–135 km thick. They however cannot explain the occurrence of local shear wave splitting, such as that beneath the Ross Sea coast, that displays an average delay time of 1.5 ± 0.08 s originated from asthenosphere estimated to be 135–225 km thick (Graw and Hansen, 2017).

Models involving mantle plumes or small-scale mantle convection have been proposed to explain the formation of the Transantarctic Mountains (Armienti and Perinelli, 2010; Faccenna et al., 2008; Kyle et al., 1992; Rocchi et al., 2002, 2003, 2005). In both cases, seismological surveys suggest low-velocity anomalies and the existence of melt in the mantle (Barklage et al., 2009; Gupta et al., 2009; Hansen et al., 2014b; Morelli and Danesi, 2004; Park et al., 2015; Sieminski et al., 2003). Melt-induced seismic anisotropies have been reported by Nakajima et al. (2005) using a quantitative interpretation of both P- and S-wave velocity structures and by Satsukawa et al. (2011) based on microstructural investigations on peridotite xenoliths. The Cr# values of the spinel in the analyzed samples was estimated as 0.15–0.31, corresponding to a $\leq 7\%$ melt (e.g., Park et al., 2020). The study area contains abundant tectonic faults that are oriented perpendicular to the direction of fast shear wave splitting and can generate a weak seismic anisotropy (Fig. 12). The observed delay time of $0.9\text{--}1.3$ s (Pondrelli and Azzara, 1998) requires seismic anisotropies of 17%–25% assuming a lithospheric mantle that is 100 km thick. The AV_S caused by trapped melts parallel to APM in this study are estimated as 10%–18% if we assume

shape ratios of between 5:5:1 and 10:10:1 and a melt fraction of 7% (Vauchez et al., 2000). We suggest therefore that the existence of melt trapped along faults can partially explain the generation of seismic anisotropy beneath northern Victoria Land. The summation of seismic anisotropy caused by the presence of both mantle peridotites (5% from J04-A5 and 8% from J04-D) and melt-pockets (10%–18%) is essential to fully explain the seismic anisotropy of 17%–25% that is estimated from 100 km thick lithospheric mantle, with an observed delay time of 0.9–1.3 s (Pondrelli and Azzara, 1998).

6. Conclusions

The NE–SW-trending S-wave splitting widely observed in northern Victoria Land, Antarctica, is usually explained by the presence of melt-pockets developed along large-scale tectonic faults or the existence of lithospheric fabric. We first report the origin of seismic anisotropies calculated directly from mantle xenoliths around Mt Melbourne in northern Victoria Land and summarize the following conclusions.

1. The studied mantle xenoliths are classified into three harzburgites and three lherzolites based on the mineral abundances of major minerals (olivine, orthopyroxene, clinopyroxene). The irregular grain boundaries of porphyroclastic olivine and clinopyroxene exsolution lamellae in porphyroclastic orthopyroxene are observed in both lithologies, but the shape-preferred orientations of both porphyroclastic olivine and orthopyroxene microstructures are characterized only in spinel lherzolites.
2. Because of a lack of structural indicators in the sample specimens, the olivine [100] and [010] are rotated into a horizontal and vertical orientations, respectively, after the EBSD measurements. The shape factor K calculated from eigenvalues defines an ambiguous [010] of olivine into a girdle or a cluster; hence, one sample is classified as an A-type olivine and the others as D-type olivine. The calculated FIAs are 51°–76°, with one sample classified as an A-type olivine and the others as D-type olivine. These consistent results using both quantitative methods provide an appropriate definition of olivine for massive mantle xenoliths that lack structural indicators.
3. Microstructures of porphyroclastic olivine (complex shape of grain boundaries) and orthopyroxene (exsolution lamellae) provide evidence for the main deformation event. The limited volume of fine-grained recrystallized crystals and the relationship between low Cr# in spinel and high Fo# in olivine are indicative of low-degree partial melting that suggests an insignificant influence of metasomatism. The dominance of D-type olivine CPOs and only one sample showing an A-type CPO are explained by multiple slip

Generation of melt-pockets along faults

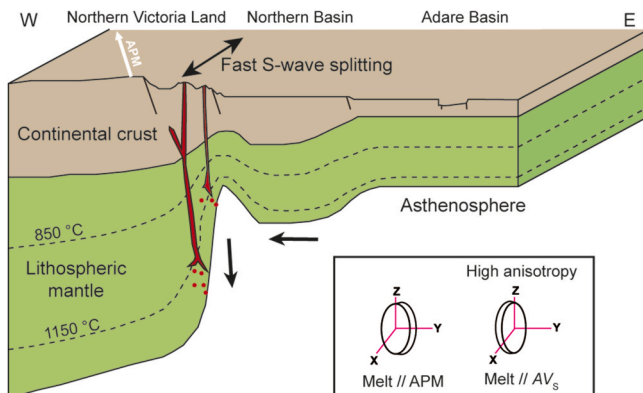


Fig. 12. Schematic model of the influence of melt pockets on anisotropy. Melt pockets (red color) parallel to the APM (white arrow) can generate 10%–18% AV_s , assuming shape ratios of 5:5:1 to 10:10:1 and 7% melt (Vauchez et al., 2000). APM = absolute plate motion (Gripp and Gordon, 2002). (For interpretation of the references to colour in this figure legend, the reader is referred to the Web version of this article.)

systems of {0kl}[100] at low temperature and high stress conditions. The mixing of mafic magmas involving 20–35% of eclogitic materials during the Ross Orogeny (550–600 Ma) and the reactivation during the opening of the West Antarctic Rift System (~120 Ma) have been suggested by highly radiogenic Os from mantle peridotites (Barker Rocks and Greene Point) in the northern part of Mt. Melbourne. These results allow the interpretation that both compressional and extensional regimes during subducting and rifting, respectively, could explain the formation of D-type olivine fabric in the study area. Relatively low estimated equilibrium temperatures of 860–920 °C calculated using a Ca-in-orthopyroxene thermometer may be explained by the ‘stagnant’ condition that is probably related with an exhumation event at low temperature and high stress mantle shear zone.

4. The averaged seismic properties of olivine aggregates and whole-rocks (olivine + orthopyroxene + clinopyroxene) are characterized by a maximum splitting of S-wave propagation parallel to olivine a -axes. With assumptions that olivine a -axes are aligned along the mantle flow to generate maximum S-wave splitting and the thickness of lithosphere should be 100 km, the observed delay time of 0.9–1.3 s beneath northern Victoria Land may be explained partially (up to 1.1 s) by the anisotropy in the peridotite xenoliths. Confirmation of the existence of melts trapped along faults is needed to explain the rest of the observed S-wave splitting. Therefore, our findings suggest the seismic anisotropy beneath northern Victoria Land can be explained by the existence of both mantle peridotites and melt-pockets along large-scaled NW–SE-trending faults. Additional microstructural studies on peridotite xenoliths from other areas should be evaluated for a more thorough understanding of the origin of the NE–SW-trending S-wave splitting beneath northern Victoria Land, Antarctica.

CRediT authorship contribution statement

Daeyeong Kim: Conceptualization, Methodology, Software, Investigation, Validation, Data curation, Writing - original draft, Writing - review & editing, Visualization. **Munjae Park:** Investigation, Writing - original draft, Writing - review & editing. **Yongcheol Park:** Funding acquisition, Writing - review & editing. **Chao Qi:** Software, Writing - original draft, Writing - review & editing. **Hwayoung Kim:** Investigation, Data curation, Visualization, Writing - review & editing. **Mi Jung Lee:** Resources, Writing - review & editing. **Katsuyoshi Michibayashi:**

Software, Writing - review & editing.

Declaration of competing interest

The authors declare that they have no known competing financial interests or personal relationships that could have appeared to influence the work reported in this paper.

Acknowledgments

The authors appreciate the technical support of Kyungtae Park and Heymi Cho for EBSD analyses. This research was supported by the Korea Polar Research Institute (KOPRI), Republic of Korea projects PE20210. The earlier version of the manuscript has been greatly improved by fruitful comments of an anonymous reviewer and Vasileios Chatzaras, and the considerate editorial work by Toru Takeshita.

Data availability

Data can be obtained via <https://doi.org/10.6084/m9.figshare.10297694> (Kim et al., 2019).

References

- Abramson, E.H., Brown, J.M., Slutsky, L.J., Zaug, J., 1997. The elastic constants of san carlos olivine to 17 GPa. *Journal of geophysical research: Solid Earth* 102, 12253–12263.
- Armenti, P., Perinelli, C., 2010. Cenozoic thermal evolution of lithospheric mantle in northern Victoria Land (Antarctica): evidences from mantle xenoliths. *Tectonophysics* 486, 28–35.
- Bai, Q., Mackwell, S.J., Kohlstedt, D.L., 1991. High-temperature creep of olivine single crystals I. Mechanical results for buffered samples. *Journal of Geophysical Research: Solid Earth* 96, 2441–2463.
- Barklage, M., Wiens, D.A., Nyblade, A., Anandakrishnan, S., 2009. Upper mantle seismic anisotropy of South Victoria Land and the Ross Sea coast, Antarctica from SKS and SKKS splitting analysis. *Geophys. J. Int.* 178, 729–741.
- Bell, T.H., Hickey, K.A., Upton, G.J.G., 1998. Distinguishing and correlating multiple phases of metamorphism across a multiply deformed region using the axes of spiral, staircase and sigmoidal inclusion trails in garnet. *J. Metamorph. Geol.* 16, 767–794.
- Ben Ismail, W., Mainprice, D., 1998. An olivine fabric database: an overview of upper mantle fabrics and seismic anisotropy. *Tectonophysics* 296, 145–157.
- Bernard, R.E., Behr, W.M., Becker, T.W., Young, D.J., 2019. Relationships between olivine CPO and deformation parameters in naturally deformed rocks and implications for mantle seismic anisotropy. *Geochemistry, geophysics, Geosystems* 20, 3469–3494.
- Boneh, Y., Morales, L.F.G., Kaminski, E., Skemer, P., 2015. Modeling olivine CPO evolution with complex deformation histories: implications for the interpretation of seismic anisotropy in the mantle. *Geochemistry, Geophysics, Geosystems* 16, 3436–3455.
- Boneh, Y., Skemer, P., 2014. The effect of deformation history on the evolution of olivine CPO. *Earth Planet Sci. Lett.* 406, 213–222.
- Borg, S.G., Stump, E., Chappell, B.W., McCulloch, M.T., Wyborn, D., Armstrong, R.L., Holloway, J.R., 1987. Granitoids of northern Victoria Land, Antarctica: implications of chemical and isotopic variations to regional crustal structure and tectonics. *Am. J. Sci.* 287, 127–169.
- Brey, G.P., Köhler, T., 1990. Geothermobarometry in four-phase lherzolites II. New thermobarometers, and practical assessment of existing thermobarometers. *J. Petrol.* 31, 1353–1378.
- Bunge, H.J., 1982. *Texture analysis in materials science: mathematical methods*. Butterworths, London.
- Bystricky, M., Kunze, K., Burlini, L., Burg, J.-P., 2000. High shear strain of olivine aggregates: rheological and seismic consequences. *Science* 290, 1564–1567.
- Cao, Y., Jung, H., Song, S., Park, M., Jung, S., Lee, J., 2015. Plastic deformation and seismic properties in fore-arc mantles: a petrofabric analysis of the yushigou harzburgites, north qilian suture zone, NW China. *J. Petrol.* 56, 1897–1944.
- Carter, N.L., Ave'Lallmann, H.G., 1970. High temperature flow of dunite and peridotite. *GSA Bulletin* 81, 2181–2202.
- Chapman, D.S., 1986. Thermal gradients in the continental crust. *Special Publications*, vol. 24. Geological Society, London, p. 63.
- Collins, M.D., Brown, J.M., 1998. Elasticity of an upper mantle clinopyroxene. *Phys. Chem. Miner.* 26, 7–13.
- Coltorti, M., Beccaluva, L., Bonadiman, C., Faccini, B., Ntaflos, T., Siena, F., 2004. Amphibole genesis via metasomatic reaction with clinopyroxene in mantle xenoliths from Victoria Land, Antarctica. *Lithos* 75, 115–139.
- Couvy, H.I.N., Frost, D.J., Heidelbach, F., Nyilas, K.N., UngáR, T.S., Mackwell, S., Cordier, P., 2004. Shear deformation experiments of forsterite at 11 GPa – 1400 °C in the multianvil apparatus. *Eur. J. Mineral.* 16, 877–889.
- DiVenere, V.J., Kent, D.V., Dalziel, I.W.D., 1994. Mid-cretaceous paleomagnetic results from marie byrd Land, west Antarctica: a test of post-100 Ma relative motion

- between east and west Antarctica. *Journal of geophysical research: Solid Earth* 99, 15115–15139.
- Duffy, T.S., Vaughan, M.T., 1988. Elasticity of enstatite and its relationship to crystal structure. *J. Geophys. Res.: Solid Earth* 93, 383–391.
- Durham, W.B., Goetze, C., 1896–1977. 1977. Plastic flow of oriented single crystals of olivine: 1. Mechanical data. *J. Geophys. Res.* 82, 5737–5753.
- Estrada, S., Läufer, A., Eckelmann, K., Hofmann, M., Gärtner, A., Linnemann, U., 2016. Continuous neoproterozoic to ordovician sedimentation at the east Gondwana margin — implications from detrital zircons of the Ross orogen in northern Victoria Land, Antarctica. *Gondwana Res.* 37, 426–448.
- Faccenna, C., Rossetti, F., Becker, T.W., Danesi, S., Morelli, A., 2008. Recent extension driven by mantle upwelling beneath the Admiralty Mountains (East Antarctica). *Tectonics* 27, TC4015.
- Falus, G., Tommasi, A., Ingrin, J., Szabó, C., 2008. Deformation and seismic anisotropy of the lithospheric mantle in the southeastern Carpathians inferred from the study of mantle xenoliths. *Earth Planet Sci. Lett.* 272, 50–64.
- Falus, G., Tommasi, A., Soustelle, V., 2011. The effect of dynamic recrystallization on olivine crystal preferred orientations in mantle xenoliths deformed under varied stress conditions. *J. Struct. Geol.* 33, 1528–1540.
- Finn, C., Moore, D., Damaske, D., Mackey, T., 1999. Aeromagnetic legacy of early Paleozoic subduction along the Pacific margin of Gondwana. *Geology* 27, 1087–1090.
- Fitzgerald, P.G., 1994. Thermochronologic constraints on post-Paleozoic tectonic evolution of the central Transantarctic Mountains, Antarctica. *Tectonics* 13, 818–836.
- Fitzgerald, P.G., Stump, E., 1997. Cretaceous and Cenozoic episodic denudation of the Transantarctic Mountains, Antarctica: new constraints from apatite fission track thermochronology in the Scott Glacier region. *J. Geophys. Res.: Solid Earth* 102, 7747–7765.
- Gibson, G.M., Wright, T.O., 1985. Importance of thrust faulting in the tectonic development of northern Victoria Land, Antarctica. *Nature* 315, 480–483.
- Grav, J.H., Hansen, S.E., 2017. Upper mantle seismic anisotropy beneath the Northern Transantarctic Mountains, Antarctica from PKS, SKS, and SKKS splitting analysis. *G-cubed* 18, 544–557.
- Green, D.H., Ringwood, A.E., 1967. The stability fields of aluminous pyroxene peridotite and garnet peridotite and their relevance in upper mantle structure. *Earth Planet Sci. Lett.* 3, 151–160.
- Gripp, A.E., Gordon, R.G., 2002. Young tracks of hotspots and current plate velocities. *Geophys. J. Int.* 150, 321–361.
- Gupta, S., Zhao, D., Rai, S.S., 2009. Seismic imaging of the upper mantle under the Erebus hotspot in Antarctica. *Gondwana Res.* 16, 109–118.
- Hansen, L.N., Zhao, Y.-H., Zimmerman, M.E., Kohlstedt, D.L., 2014a. Protracted fabric evolution in olivine: implications for the relationship among strain, crystallographic fabric, and seismic anisotropy. *Earth Planet Sci. Lett.* 387, 157–168.
- Hansen, L.N., Zimmerman, M.E., Kohlstedt, D.L., 2012. The influence of microstructure on deformation of olivine in the grain-boundary sliding regime. *Journal of Geophysical Research: solid Earth* 117, B09201.
- Hansen, S.E., Grav, J.H., Kenyon, L.M., Nyblade, A.A., Wiens, D.A., Aster, R.C., Huerta, A.D., Anandakrishnan, S., Wilson, T., 2014b. Imaging the Antarctic mantle using adaptively parameterized P-wave tomography: evidence for heterogeneous structure beneath West Antarctica. *Earth Planet Sci. Lett.* 408, 66–78.
- Hess, H.H., 1964. Seismic anisotropy of the uppermost mantle under oceans. *Nature* 203, 629–631.
- Holtzman, B.K., Kohlstedt, D.L., Zimmerman, M.E., Heidelbach, F., Hiraga, T., Hustoft, J., 2003. Melt segregation and strain partitioning: implications for seismic anisotropy and mantle flow. *Science* 301, 1227.
- Jung, H., Karato, S.-i., 2001. Water-induced fabric transitions in olivine. *Science* 293, 1460–1463.
- Jung, H., Katayama, I., Jiang, Z., Hiraga, T., Karato, S., 2006. Effect of water and stress on the lattice-preferred orientation of olivine. *Tectonophysics* 421, 1–22.
- Karato, S.-i., 2008. Lattice-preferred Orientation. In: Karato, S.-i. (Ed.), *Deformation of Earth Materials: an Introduction to the Rheology of Solid Earth*. Cambridge University Press, Cambridge, pp. 262–267.
- Karato, S.-i., Jung, H., Katayama, I., Skemer, P., 2008. Geodynamic significance of seismic anisotropy of the upper mantle: new insights from laboratory studies. *Annu. Rev. Earth Planet Sci.* 36, 59–95.
- Kim, D., Wallis, S., Endo, S., Ree, J.-H., 2016. Seismic properties of lawsonite eclogites from the southern Motagua fault zone, Guatemala. *Tectonophysics* 677–678, 88–98.
- Katayama, I., Hirauchi, K.-i., Michibayashi, K., Ando, J.-i., 2009. Trench-parallel anisotropy produced by serpentine deformation in the hydrated mantle wedge. *Nature* 461, 1114–1117.
- Katayama, I., Jung, H., Karato, S.-i., 2004. New type of olivine fabric from deformation experiments at modest water content and low stress. *Geology* 32, 1045–1048.
- Katayama, I., Karato, S.-i., 2006. Effect of temperature on the B- to C-type olivine fabric transition and implication for flow pattern in subduction zones. *Phys. Earth Planet. In.* 157, 33–45.
- Kim, T., Kim, Y., Cho, M., Lee, J.I., 2019. P-T evolution and episodic zircon growth in barroisite eclogites of the Lanterman Range, northern Victoria Land, Antarctica. *J. Metamorph. Geol.* 37, 509–537.
- Kumamoto, K.M., Warren, J.M., Hansen, L.N., 2019. Evolution of the josephine peridotite shear zones: 2. Influences on Olivine CPO Evolution. *Journal of Geophysical Research: Solid Earth* 124, 12763–12781.
- Kyle, P.R., 1990. A McMurdo volcanic Group western Ross embayment. *Volcanoes of the antarctic plate and southern oceans*, pp. 18–145.
- Kyle, P.R., Moore, J.A., Thirlwall, M.F., 1992. Petrologic evolution of anorthoclase phonolite lavas at mount erebus, Ross island, Antarctica. *J. Petrol.* 33, 849–875.
- Lee, M.J., Lee, J.I., 2017. Holocene eruptive history of Mt. Melbourne volcano, Antarctica: insights from tephra layers recorded from Talos Dome ice core. *J. Geol. Soc. Korea* 53, 509–519.
- Long, M.D., 2013. Constraints on subduction geodynamics from seismic anisotropy. *Rev. Geophys.* 51, 76–112.
- Long, M.D., Silver, P.G., 2009. Shear wave splitting and mantle anisotropy: measurements, interpretations, and new directions. *Surv. Geophys.* 30, 407–461.
- Luyendyk, B., Cisowski, S., Smith, C., Richard, S., Kimbrough, D., 1996. Paleomagnetic study of the northern ford ranges, western marie byrd Land, west Antarctica: motion between west and east Antarctica. *Tectonics* 15, 122–141.
- Lyon, G.L., 1986. Stable isotope stratigraphy of ice cores and the age of the last eruption at Mount Melbourne, Antarctica. *N. Z. J. Geol. Geophys.* 29, 135–138.
- Mackwell, S.J., Kohlstedt, D.L., Paterson, M.S., 1985. The role of water in the deformation of olivine single crystals. *Journal of Geophysical Research: Solid Earth* 90, 11319–11333.
- Mainprice, D., 1990. A FORTRAN program to calculate seismic anisotropy from the lattice preferred orientation of minerals. *Comput. Geosci.* 16, 385–393.
- Mainprice, D., 2007. Seismic anisotropy of the deep Earth from a mineral and rock physics perspective. *Treatise of Geophysics* 2, 437–491.
- Mainprice, D., Hielscher, R., Schaeben, H., 2011. Calculating anisotropic physical properties from texture data using the MTEX open-source package. *Special Publications*, vol. 360. Geological Society, London, pp. 175–192.
- Mainprice, D., Silver, P.G., 1993. Interpretation of SKS-waves using samples from the subcontinental lithosphere. *Phys. Earth Planet. In.* 78, 257–280.
- Manthilake, M.A.G.M., Miyajima, N., Heidelbach, F., Soustelle, V., Frost, D.J., 2013. The effect of aluminum and water on the development of deformation fabrics of orthopyroxene. *Contrib. Mineral. Petrol.* 165, 495–505.
- Martin, A.P., Price, R.C., Cooper, A.F., McCammon, C.A., 2015. Petrogenesis of the rifted southern Victoria Land lithospheric mantle, Antarctica, inferred from petrography, geochemistry, thermobarometry and oxybarometry of peridotite and pyroxenite xenoliths from the mount morning eruptive centre. *J. Petrol.* 56, 193–226.
- Maruyama, G., Hiraga, T., 2017. Grain- to multiple-grain-scale deformation processes during diffusion creep of forsterite + diopside aggregate: 1. Direct observations. *Journal of Geophysical Research: Solid Earth* 122, 5890–5915.
- Melchiorre, M., Coltorti, M., Bonadiman, C., Faccini, B., O'Reilly, S.Y., Pearson, N.J., 2011. The role of eclogite in the rift-related metasomatism and Cenozoic magmatism of Northern Victoria Land, Antarctica. *Lithos* 124, 319–330.
- Michibayashi, K., Mainprice, D., 2004. The role of pre-existing mechanical anisotropy on shear zone development within oceanic mantle lithosphere: an example from the Oman ophiolite. *J. Petrol.* 45, 405–414.
- Michibayashi, K., Mainprice, D., Fujii, A., Uehara, S., Shinkai, Y., Kondo, Y., Ohara, Y., Ishii, T., Fryer, P., Bloomer, S.H., Ishiwatari, A., Hawkins, J.W., Ji, S., 2016. Natural olivine crystal-fabrics in the western Pacific convergence region: a new method to identify fabric type. *Earth Planet Sci. Lett.* 443, 70–80.
- Michibayashi, K., Tasaka, M., Ohara, Y., Ishii, T., Okamoto, A., Fryer, P., 2007. Variable microstructure of peridotite samples from the southern Mariana Trench: evidence of a complex tectonic evolution. *Tectonophysics* 444, 111–118.
- Miyazaki, T., Sueyoshi, K., Hiraga, T., 2013. Olivine crystals align during diffusion creep of Earth's upper mantle. *Nature* 502, 321–326.
- Moore, A.C., 1970. Descriptive terminology for the textures of rocks in granulite facies terrains. *Lithos* 3, 123–127.
- Morales, L.F.G., Tommasi, A., 2011. Composition, textures, seismic and thermal anisotropies of xenoliths from a thin and hot lithospheric mantle (Summit Lake, southern Canadian Cordillera). *Tectonophysics* 507, 1–15.
- Morelli, A., Danesi, S., 2004. Seismological imaging of the Antarctic continental lithosphere: a review. *Global Planet. Change* 42, 155–165.
- Nakajima, J., Takai, Y., Hasegawa, A., 2005. Quantitative analysis of the inclined low-velocity zone in the mantle wedge of northeastern Japan: a systematic change of melt-filled pore shapes with depth and its implications for melt migration. *Earth Planet Sci. Lett.* 234, 59–70.
- Nardini, I., Armienti, P., Rocchi, S., Dallai, L., Harrison, D., 2009. Sr-Nd-Pb-He-O isotope and geochemical constraints on the genesis of cenozoic magmas from the West Antarctic Rift. *J. Petrol.* 50, 1359–1375.
- Nathan, S., Schulte, F.J., 1967. Recent thermal and volcanic activity on mount Melbourne, northern Victoria Land, Antarctica. *N. Z. J. Geol. Geophys.* 10, 422–430.
- Nazé, L., Van Dusen, J.-C., Doukhan, J.-C., Doukhan, N., 1986. Défauts de réseau et plasticité cristalline dans les pyroxènes : une revue. *Bull. Mineral.* 377–394.
- Nicolas, A., Christensen, N.I., 1987. Formation of anisotropy in upper mantle peridotites - a review. In: Fuchs, K., Froidevaux, C. (Eds.), *Composition, Structure and Dynamics of the Lithosphere-Asthenosphere System*. AGU, Washington D.C, pp. 111–123.
- Panter, K.S., Castillo, P., Krans, S., Deering, C., McIntosh, W., Valley, J.W., Kitajima, K., Kyle, P., Hart, S., Blusztajn, J., 2018. Melt origin across a rifted continental margin: a case for subduction-related metasomatic agents in the lithospheric source of alkaline basalt, NW Ross Sea, Antarctica. *J. Petrol.* 59, 517–558.
- Park, M., Jung, H., Kil, Y., 2014. Petrofabrics of olivine in a rift axis and rift shoulder and their implications for seismic anisotropy beneath the Rio Grande rift. *Isl. Arc* 23, 299–311.
- Park, M., Kil, Y., Jung, H., 2020. Evolution of deformation fabrics related to petrogenesis of upper mantle xenoliths beneath the Baekdusan volcano. *Minerals* 10, 831.
- Park, Y., Yoo, H.-J., Lee, W.-S., Lee, C.-K., Lee, J., Park, H., Kim, J., Kim, Y., 2015. P-wave velocity structure beneath Mt. Melbourne in northern Victoria Land, Antarctica: evidence of partial melting and volcanic magma sources. *Earth Planet Sci. Lett.* 432, 293–299.
- Passchier, C., Trouw, R.J., 2005. *Microtectonics*. Springer Verlag, Berlin, Heidelberg.
- Pelorosso, B., Bonadiman, C., Coltorti, M., Faccini, B., Melchiorre, M., Ntaflos, T., Gregoire, M., 2016. Pervasive, tholeiitic refertilisation and heterogeneous

- metasomatism in Northern Victoria Land lithospheric mantle (Antarctica). *Lithos* 248–251, 493–505.
- Perinelli, C., Armienti, P., Dallai, L., 2006. Geochemical and O-isotope constraints on the evolution of lithospheric mantle in the Ross Sea rift area (Antarctica). *Contrib. Mineral. Petrol.* 151, 245–266.
- Perinelli, C., Armienti, P., Dallai, L., 2011. Thermal evolution of the lithosphere in a rift environment as inferred from the geochemistry of mantle cumulates, northern Victoria Land, Antarctica. *J. Petrol.* 52, 665–690.
- Perinelli, C., Orlando, A., Conte, A.M., Armienti, P., Borrini, D., Faccini, B., Misiti, V., 2008. Metasomatism induced by alkaline magma in the upper mantle of northern Victoria Land (Antarctica): an experimental approach. *Geol. Soc. Lond. Special Publ.* 293, 279.
- Pondrelli, S., Azzara, R., 1998. Upper mantle anisotropy in Victoria Land (Antarctica). *Pure Appl. Geophys.* 151, 433–442.
- Pondrelli, S., Margheriti, L., Danesi, S., 2006. Seismic Anisotropy beneath Northern Victoria Land from SKS Splitting Analysis. In: Füllerer, D.K., Damaske, D., Kleinschmidt, G., Miller, H., Tessensohn, F. (Eds.), *Antarctica: Contributions to Global Earth Sciences*. Springer Berlin Heidelberg, Berlin, Heidelberg, pp. 155–161.
- Qi, C., Hansen, L.N., Wallis, D., Holtzman, B.K., Kohlstedt, D.L., 2018. Crystallographic preferred orientation of olivine in sheared partially molten rocks: the source of the “a-c switch”. *Geochemistry, geophysics, Geosystems* 19, 316–336.
- Raterson, P., Chen, J., Li, L., Weidner, D., Cordier, P., 2007. Pressure-induced slip-system transition in forsterite: single-crystal rheological properties at mantle pressure and temperature. *Am. Mineral.* 92, 1436–1445.
- Rocchi, S., Armienti, P., D’Orazio, M., Tonarini, S., Wijibrans, J.R., Di Vincenzo, G., 2002. Cenozoic magmatism in the western Ross embayment: role of mantle plume versus plate dynamics in the development of the West Antarctic Rift system. *J. Geophys. Res.: Solid Earth* 107, 2195.
- Rocchi, S., Armienti, P., Di Vincenzo, G., 2005. No Plume, No Rift Magmatism in the West Antarctic Rift. In: Foulger, G.R., Natland, J.H., Presnall, D.C., Anderson, D.L. (Eds.), *Plates, Plumes and Paradigms: Geological Society of America Special Paper*, 388. Geological Society of America, pp. 435–447.
- Rocchi, S., Storti, F., Di Vincenzo, G., Rossetti, F., 2003. Intrapllate strike-slip tectonics as an alternative to mantle plume activity for the Cenozoic rift magmatism in the Ross Sea region, Antarctica. *Geological Society, London, Spec. Publ.* 210, 145.
- Rocchi, S., Tonarini, S., Armienti, P., Innocenti, F., Manetti, P., 1998. Geochemical and isotopic structure of the early Palaeozoic active margin of Gondwana in northern Victoria Land, Antarctica. *Tectonophysics* 284, 261–281.
- Salimbeni, S., Pondrelli, S., Danesi, S., Morelli, A., 2010. Seismic anisotropy of the Victoria Land region, Antarctica. *Geophys. J. Int.* 182, 421–432.
- Satsukawa, T., Michibayashi, K., 2014. Flow in the uppermost mantle during back-arc spreading revealed by Ichinomegata peridotite xenoliths, NE Japan. *Lithos* 189, 89–104.
- Satsukawa, T., Michibayashi, K., Anthony, E.Y., Stern, R.J., Gao, S.S., Liu, K.H., 2011. Seismic anisotropy of the uppermost mantle beneath the Rio Grande rift: evidence from Kilbourne Hole peridotite xenoliths, New Mexico. *Earth Planet Sci. Lett.* 311, 172–181.
- Savage, M.K., 1999. Seismic anisotropy and mantle deformation: what have we learned from shear wave splitting? *Rev. Geophys.* 37, 65–106.
- Schmidt, D.L., Rowley, P.D., 1986. Continental rifting and transform faulting along the jurassic transantarctic rift, Antarctica. *Tectonics* 5, 279–291.
- Sieminski, A., Debaille, E., Lévéque, J.-J., 2003. Seismic evidence for deep low-velocity anomalies in the transition zone beneath West Antarctica. *Earth Planet Sci. Lett.* 216, 645–661.
- Silver, P.G., 1996. Seismic anisotropy beneath the continents: probing the depths of geology. *Annu. Rev. Earth Planet Sci.* 24, 385–432.
- Skemer, P., Hansen, L.N., 2016. Inferring upper-mantle flow from seismic anisotropy: an experimental perspective. *Tectonophysics* 668–669, 1–14.
- Skemer, P., Katayama, I., Jiang, Z., Karato, S.-i., 2005. The misorientation index: development of a new method for calculating the strength of lattice-preferred orientation. *Tectonophysics* 411, 157–167.
- Soustelle, V., Manthilake, G., 2017. Deformation of olivine-orthopyroxene aggregates at high pressure and temperature: implications for the seismic properties of the asthenosphere. *Tectonophysics* 694, 385–399.
- Soustelle, V., Tommasi, A., Demouchy, S., Franz, L., 2013. Melt-rock interactions, deformation, hydration and seismic properties in the sub-arc lithospheric mantle inferred from xenoliths from seamounts near Lihir, Papua New Guinea. *Tectonophysics* 608, 330–345.
- Soustelle, V., Tommasi, A., Demouchy, S., Ionov, D.A., 2010. Deformation and fluid–rock interaction in the supra-subduction mantle: microstructures and water contents in peridotite xenoliths from the avacha volcano, kamchatka. *J. Petrol.* 51, 363–394.
- Storey, B.C., Alabaster, T., 1991. Tectonomagmatic controls on Gondwana break-up models: evidence from the proto-pacific margin of Antarctica. *Tectonics* 10, 1274–1288.
- Stump, E., Fitzgerald, P.G., 1992. Episodic uplift of the transantarctic Mountains. *Geology* 20, 161–164.
- Sundberg, M., Cooper, R.F., 2008. Crystallographic preferred orientation produced by diffusional creep of harzburgite: effects of chemical interactions among phases during plastic flow. *Journal of Geophysical Research: solid Earth* 113, B12208.
- Tommasi, A., Mainprice, D., Canova, G., Chastel, Y., 2000. Viscoplastic self-consistent and equilibrium-based modeling of olivine lattice preferred orientations: implications for the upper mantle seismic anisotropy. *J. Geophys. Res.: Solid Earth* 105, 7893–7908.
- Tommasi, A., Tikoff, B., Vauchez, A., 1999. Upper mantle tectonics: three-dimensional deformation, olivine crystallographic fabrics and seismic properties. *Earth Planet Sci. Lett.* 168, 173–186.
- Tommasi, A., Vauchez, A., 2015. Heterogeneity and anisotropy in the lithospheric mantle. *Tectonophysics* 661, 11–37.
- Tommasi, A., Vauchez, A., Daudré, B., 1995. Initiation and propagation of shear zones in a heterogeneous continental lithosphere. *J. Geophys. Res.: Solid Earth* 100, 22083–22101.
- Vauchez, A., Tommasi, A., Barruol, G., Maumus, J., 2000. Upper mantle deformation and seismic anisotropy in continental rifts. *Phys. Chem. Earth Solid Earth Geodes.* 25, 111–117.
- Vollmer, F.W., 1990. An application of eigenvalue methods to structural domain analysis. *GSA Bulletin* 102, 786–791.
- Warren, J.M., Hirth, G., Kelemen, P.B., 2008. Evolution of olivine lattice preferred orientation during simple shear in the mantle. *Earth Planet Sci. Lett.* 272, 501–512.
- Wells, P.R.A., 1977. Pyroxene thermometry in simple and complex systems. *Contrib. Mineral. Petrol.* 62, 129–139.
- Whitney, D.L., Evans, B.W., 2010. Abbreviations for names of rock-forming minerals. *Am. Mineral.* 95, 185–187.
- Zhang, S., Karato, S.-i., 1995. Lattice preferred orientation of olivine aggregates deformed in simple shear. *Nature* 375, 774–777.
- Zhang, S., Karato, S.-i., Fitz Gerald, J., Faul, U.H., Zhou, Y., 2000. Simple shear deformation of olivine aggregates. *Tectonophysics* 316, 133–152.